

School of Natural Sciences and Mathematics

Propagation Characteristics of Plasmaspheric Hiss: Van Allen Probe Observations and Global Empirical Models

UT Dallas Author(s):

Lunjin Chen

Rights:

©2017 American Geophysical Union

Citation:

Yu, J., L. Y. Li, J. B. Cao, L. Chen, et al. 2017. "Propagation characteristics of plasmaspheric hiss: Van Allen probe observations and global empirical models." *Journal of Geophysical Research--Space Physics* 122(4), doi:10.1002/2016JA023372

This document is being made freely available by the Eugene McDermott Library of the University of Texas at Dallas with permission of the copyright owner. All rights are reserved under United States copyright law unless specified otherwise.

RESEARCH ARTICLE

10.1002/2016JA023372

Key Points:

- Global hiss wave amplitudes and wave normal angles (WNAs) are observed by Van Allen Probe A during different-intensity substorm activities
- The propagation angles of hiss waves have no strong dependence on substorm activity in most regions, except for the nightside low L-region
- The global empirical models of hiss propagation angles and amplitudes are developed based on the Van Allen Probe observations

Correspondence to:

L. Y. Li,
lyli_ssri@buaa.edu.cn

Citation:

Yu, J., L. Y. Li, J. B. Cao, L. Chen, J. Wang, and J. Yang (2017), Propagation characteristics of plasmaspheric hiss: Van Allen Probe observations and global empirical models, *J. Geophys. Res. Space Physics*, 122, 4156–4167, doi:10.1002/2016JA023372.

Received 21 AUG 2016

Accepted 6 MAR 2017

Accepted article online 13 MAR 2017

Published online 12 APR 2017

Propagation characteristics of plasmaspheric hiss: Van Allen Probe observations and global empirical models

J. Yu¹ , L. Y. Li¹ , J. B. Cao¹ , L. Chen² , J. Wang¹ , and J. Yang¹ 

¹School of Space and Environment, Beihang University, Beijing, China, ²Department of Physics, University of Texas at Dallas, Richardson, Texas, USA

Abstract Based on the Van Allen Probe A observations from 1 October 2012 to 31 December 2014, we develop two empirical models to respectively describe the hiss wave normal angle (WNA) and amplitude variations in the Earth's plasmasphere for different substorm activities. The long-term observations indicate that the plasmaspheric hiss amplitudes on the dayside increase when substorm activity is enhanced (*AE* index increases), and the dayside hiss amplitudes are greater than the nightside. However, the propagation angles (WNAs) of hiss waves in most regions do not depend strongly on substorm activity, except for the intense substorm-induced increase in WNAs in the nightside low L-region. The propagation angles of plasmaspheric hiss increase with increasing magnetic latitude or decreasing radial distance (L-value). The global hiss WNAs (the power-weighted averages in each grid) and amplitudes (medians) can be well reproduced by our empirical models.

1. Introduction

Plasmaspheric hiss is a kind of structureless electromagnetic emission from 20 Hz to a few kHz inside the high-density plasmasphere or plume [Chan and Holzer, 1976; Meredith et al., 2004; Cao et al., 2005]. The extremely low frequency (ELF) hiss waves are probably amplified through the cyclotron resonance with anisotropic suprathermal electrons or the penetration of whistler mode chorus waves [Meredith et al., 2004; Bortnik et al., 2008; Chen et al., 2012; Zhima et al., 2013; Li et al., 2015a]. Since whistler mode hiss waves can scatter relativistic electrons (>0.5 MeV) into the loss cone [Summers et al., 2007a, 2007b; Cao et al., 2007; Xiao et al., 2010; L. Y. Li et al., 2008, 2013; Tu et al., 2013], they are often used to account for the relativistic electron loss in the slot region (L ~ 2–3) [Lyons et al., 1972; Meredith et al., 2007]. Moreover, plasmaspheric hiss can also cause the slow decay of an unusual narrow ring of relativistic electrons near L ~ 3.2 [Thorne et al., 2013]. In comparison with electromagnetic ion cyclotron (EMIC) waves [Li et al., 2016], hiss waves can scatter more relativistic electrons at almost all pitch angles and thus promote the electron loss when there are EMIC waves [Yu et al., 2015].

During the wave particle resonant interactions, the electron loss time scales (a few hours to tens of days) depend on the electron energy, ambient plasma density, ambient magnetic field strength, wave amplitude, and wave normal angle (WNA) [Meredith et al., 2007; Ni et al., 2014]. On the one hand, the pitch angle diffusion coefficient of resonant electrons is proportional to the wave amplitude [Summers et al., 2007a, 2007b]. On the other hand, the oblique whistler mode waves (e.g., hiss) can cause faster electron pitch angle scattering than the parallel waves with the same amplitude [Li et al., 2014], and the WNA effect is pronounced for the low pitch angle electrons above 1 MeV [Artemyev et al., 2012; Gao et al., 2015]. Therefore, both hiss wave amplitude and WNA are very important for the radiation belt modeling.

The amplitudes of global hiss waves have been extensively investigated [Meredith et al., 2004; Kim et al., 2015; Li et al., 2015b]. Based on the Van Allen Probe observations, Spasojevic et al. [2015] established the global empirical models of hiss wave amplitudes. Although the propagation characteristics of whistler mode waves have also been observed by Cluster [Agapitov et al., 2013], chorus waves are distinguished from hiss waves merely based on a frequency boundary (above or below $0.1f_{ce}$, where f_{ce} is the electron cyclotron frequency). Unfortunately, the highest frequency of hiss waves is often the same as the lowest frequency of low-band chorus waves in most cases. As one case, the frequency overlap of hiss and chorus waves is shown in Figure 1f. Since hiss waves and chorus waves have similar propagation and polarization (i.e., whistler mode wave properties), we cannot distinguish them merely based on a simple frequency

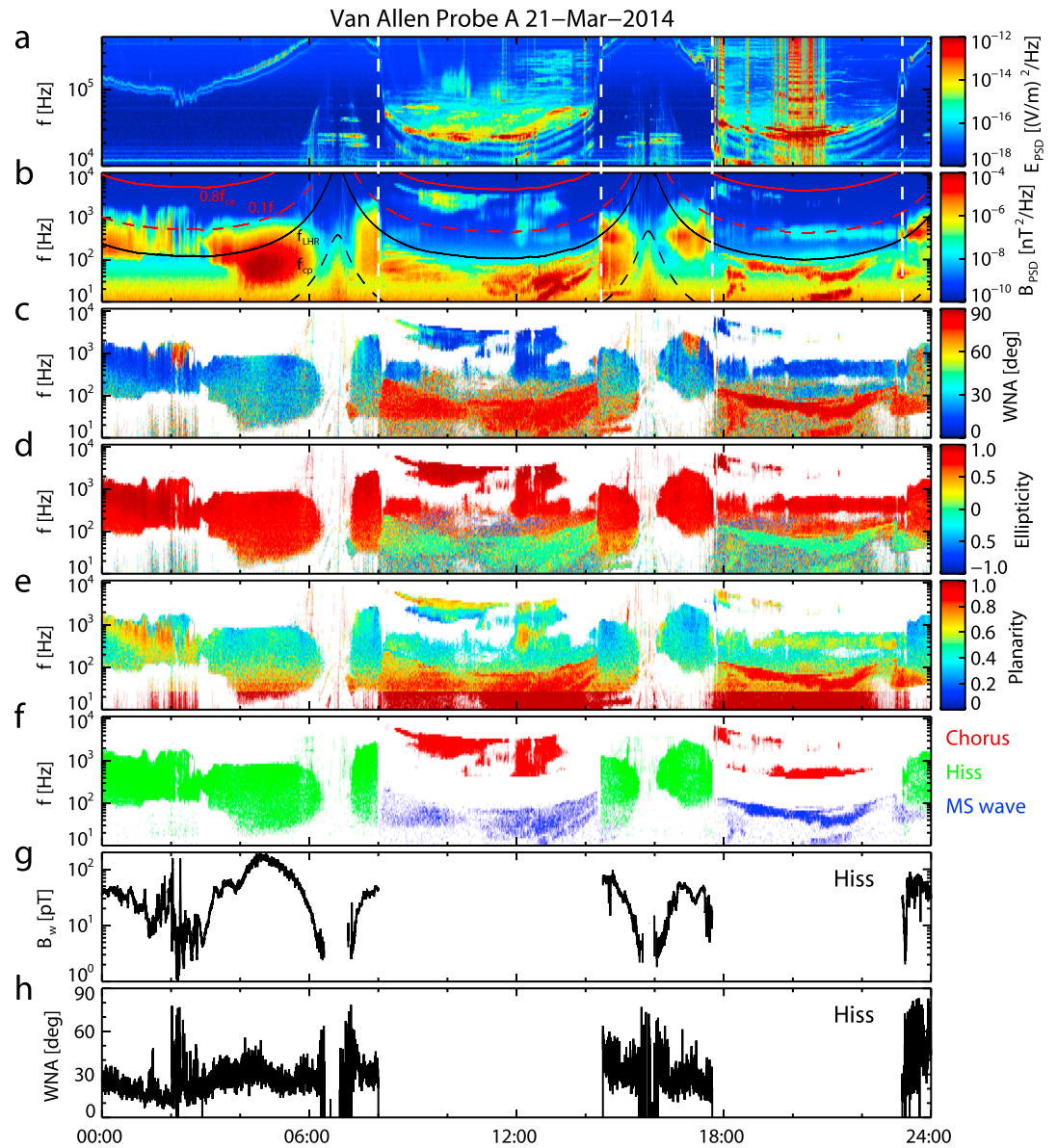


Figure 1. (a) Power spectral density of electric field from the high-frequency receiver (HFR) on board Van Allen Probe A. (b) Power spectral density of magnetic field from the waveform receiver (WFR). (c–e) Wave normal angle (WNA), ellipticity, and planarity. (f) Wave frequency ranges (hiss: red dots, chorus: green dots, magnetosonic (MS) waves: blue dots). (g) Amplitude of hiss waves. (h) The power-weighted average of hiss WNAs. f_{ce} and f_{cp} are the electron and proton cyclotron frequencies, respectively. f_{LHR} is the lower hybrid resonance frequency. The vertical dash lines mark the plasmapause location.

boundary instead of plasmapause location. Moreover, the propagation angle models of global hiss waves are not established so far.

In this paper, we reinvestigate the amplitude and WNA of global hiss waves and develop the first empirical model to describe the hiss propagation angle variation inside the plasmasphere. The hiss waves are measured by the Electric and Magnetic Field Instrument Suite and Integrated Science (EMFISIS) [Kletzing et al., 2013] on board Van Allen Probe A, and they are strictly distinguished from chorus waves based on the spatial relationship between wave emission region and plasmapause location. The plasmapause identification and data process methods are introduced in section 2. The statistical results are displayed in section 3. The empirical models of global hiss waves are established in section 4. The discussions are performed in section 5, and the conclusions are summarized in section 6.

2. Plasmopause Identification and Data Process Methods

Van Allen Probe A was launched on 24 August 2012. Its EMFISIS instrument mainly measures wideband electromagnetic waves in Earth's plasmasphere and outer radiation belt region, and its high-frequency receiver (HFR) records the electric spectral intensity in the frequency range of ~10–400 kHz. Figure 1a shows the HFR spectra measured by the Van Allen Probe A on 21 March 2014. In the HFR spectrum, the upper hybrid resonance (UHR) band is the most intense [Spasojevic *et al.*, 2015]. Although the electron plasma density can be estimated through the UHR frequency [Kurth *et al.*, 2015], the electron density is lacking most of the time and thus not used to identify the plasmopause location.

The plasmopause location can be clearly identified when there are sharp jumps in UHR curves. If the UHR curves have no sharp jump, then electrostatic electron cyclotron harmonic (ECH) waves and/or whistler mode chorus waves can be used to distinguish the low-density plasma trough from the high-density plasmasphere. Since ECH waves and chorus waves are usually excited outside the plasmopause [Meredith *et al.*, 2004, 2012; Li *et al.*, 2015a], the satellite (Van Allen Probe A) is outside the plasmopause when it observes intense ECH waves and/or whistler mode chorus waves. The power spectrum density (PSD) of chorus waves has a deep gap around $0.5f_{ce}$ (the electron cyclotron frequency $f_{ce} = eB/(2\pi m_e c)$), and their frequency ($f_{cw} \sim 0.1-0.8 f_{ce}$) has significantly altitudinal (L or B) variation. However, the frequency of plasmaspheric hiss ($f_{hw} \sim 0.02-4$ kHz) has no altitudinal (L or B) dependence, and their PSD has also no regular gap. The hiss waves merely exist inside the high-density plasmasphere/plume (e.g., in the first Radiation Belt Storm Probes pass region in Figure 1a). Moreover, the frequency of UHR inside the plasmopause is also much higher than that outside the plasmopause, owing to the larger B and higher plasma density inside the plasmasphere.

Based on the plasmopause location and the wave properties, we can sort out the hiss waves from the chorus waves. Figures 1b–1e show the PSD (B_{PSD}) of magnetic field and the characteristic parameters (WNA, ellipticity, and planarity) of waves (~0.01–12 kHz). The WNA, ellipticity, and planarity are from the Level 2 data set of the waveform receiver (WFR) integrated in EMFISIS [Kletzing *et al.*, 2013], and they are calculated through the singular value decomposition method [Santolik *et al.*, 2003]. Inside the plasmopause, the ELF electromagnetic waves (~0.02–1 kHz) are identified as plasmaspheric hiss when they have a planarity greater than 0.2 and an ellipticity greater than 0.7 [Li *et al.*, 2015b]. Although whistler mode chorus waves (~0.1–0.8 f_{ce}) have also a large planarity (>0.2) and ellipticity (>0.7), they mainly exist outside the plasmopause [Li *et al.*, 2015a]. Unlike the hiss and chorus waves, magnetosonic (MS) waves can exist either inside the plasmasphere or outside the plasmopause and their propagation is highly oblique (WNA > 80°) and their polarized ellipticity is linear (between ±0.2) [Ma *et al.*, 2016]. The frequency of MS waves is between proton gyrofrequency (f_{cp}) and lower hybrid resonance frequency (f_{LHR}).

In Figure 1f, the green, red, and blue dots show the frequency ranges of three kinds of waves, respectively. In most cases, whistler mode hiss waves and chorus waves can have similar WNA (Figure 1c), similar ellipticity (Figure 1d), similar planarity (Figure 1e), and the same frequency (Figure 1f). Therefore, we can distinguish them according to the spatial relationship between wave emission region and plasmopause location. At each sample time (i), the hiss wave amplitude (B_{wi}) is a function of its PSD ($B_{PSD}(f)$) at each frequency (f) and

$$B_{wi}^2 = \int_{f_{min}}^{f_{max}} B_{PSD}(f) df |_i \quad (1)$$

where f_{max} and f_{min} are the maximum and minimum frequencies of the measured hiss waves, respectively. Figure 1g displays the hiss wave amplitudes ($B_w = B_{wi}$) at a different time. The weak wave powers ($B_{PSD} < 10^{-9}$ nT²/Hz) are comparable to the noise level (displayed in Figure 1b), and they are ignored in our calculations.

Since the larger power hiss waves can cause faster electron pitch angle diffusion and loss, the wave normal angle of the larger power waves is significant for the radiation belt electron dynamics. At each sample time (i), the wave normal angle (WNA_{*i*}) is a weighted average by the wave power and

$$WNA_i = \frac{\int_{f_{min}}^{f_{max}} WNA(f) B_{PSD}(f) df |_i}{\int_{f_{min}}^{f_{max}} B_{PSD}(f) df |_i} \quad (2)$$

Figure 1h displays the power-weighted WNA (=WNA_{*i*}) of hiss waves measured at each sample time.

Based on the wave parameters measured by Van Allen Probe A, we obtained the amplitude and WNA of global hiss waves during the 26 months from 1 October 2012 to 31 December 2014. Previous studies indicate that intense substorm activity can inject anisotropic suprathermal electrons and excite whistler mode chorus waves [W. Li *et al.*, 2008], and whistler mode hiss waves can be amplified through the cyclotron resonance with anisotropic suprathermal electrons [Meredith *et al.*, 2004; Chen *et al.*, 2012] or the penetration of chorus waves [Bortnik *et al.*, 2008; Chen *et al.*, 2012; Li *et al.*, 2015a]. Consequently, the amplitudes of hiss and chorus waves are largely substorm dependent [Meredith *et al.*, 2004, 2012; Li *et al.*, 2015b]. Here we adopt *AE* index as a proxy of substorm intensity [Li *et al.*, 2009]. $AE < 100$ nT for quiet times or weak substorms, $100 \leq AE < 300$ nT for moderate substorms, and $AE \geq 300$ nT for intense substorms.

To obtain the substorm-dependent hiss variation, the hiss wave amplitude and WNA are chosen for different *AE* levels, and then the chosen hiss data are put into each bin ($L \sim 0.2$, $MLT \sim 1.0$ h, and $MLAT \sim 2.0^\circ$, where *MLT* is magnetic local time and *MLAT* is magnetic latitude). In each bin with sample numbers (n), the median (B_w) of the hiss wave amplitudes can reflect the hiss wave intensity and the power-weighted average $\langle WNA \rangle$ of hiss WNAs is calculated through

$$\langle WNA \rangle = \frac{\sum_{i=1}^n \int_{f_{\min}}^{f_{\max}} WNA(f) B_{\text{PSD}}(f) df |_i}{\sum_{i=1}^n \int_{f_{\min}}^{f_{\max}} B_{\text{PSD}}(f) df |_i} \quad (3)$$

3. Statistical Results

Figure 2 shows the global (*L*-*MLT*) distributions of hiss wave amplitudes (median B_w) and WNAs (i.e., the power-weighted average $\langle WNA \rangle$) during different-intensity substorm (*AE*) activities. The small disk-like panels show statistical sample numbers in each bin. During quiet times or weak substorm activity ($AE < 100$ nT), there are still intense hiss waves ($20 \text{ pT} \leq B_w \leq 40 \text{ pT}$) inside the dayside plasmasphere ($MLT \sim 08:00\text{--}18:00$) and the dayside hiss amplitudes are larger than those on the nightside (Figures 2a and 2g). However, the *MLT* distribution of hiss WNAs is relatively uniform (Figures 2d and 2j). The WNAs of hiss waves have significant latitudinal and radial variations. The equatorial hiss WNAs ($|MLAT| \leq 10^\circ$) are less than or equal to 30° (Figure 2d), whereas the midlatitude hiss WNAs ($|MLAT| > 10^\circ$) are mostly larger than 30° in the plasmaspheric region of $L \leq 5$ (Figure 2j). At different *MLTs*, the hiss WNAs tend to increase with decreasing radial distance (i.e., the decreasing *L*-value).

During the moderate and intense substorm activities ($100 \leq AE < 300$ nT and $AE \geq 300$ nT), the hiss wave amplitudes increase remarkably on the dawnside and entire dayside ($30 \text{ pT} \leq B_w \leq 100 \text{ pT}$ in the range of $MLT \sim 05:00\text{--}17:00$ in Figures 2b, 2c, 2h, and 2i), indicating that the enhanced substorm activities cause the amplifications of the dawnside and dayside hiss waves. However, the intense substorm activities (i.e., the increasing *AE*) do not effectively change the hiss wave amplitudes on the nightside ($MLT \sim 18:00\text{--}04:00$). Consequently, the day-night asymmetry of hiss wave amplitudes becomes more prominent during intense substorm activities (i.e., high *AE*). The substorm dependent variation of hiss wave amplitudes is consistent with previous statistical results [Meredith *et al.*, 2004; Li *et al.*, 2015b]. Interestingly, during quiet times, the hiss wave amplitudes are the largest in the sector from noon to afternoon (indicated by Figures 2a and 2g), whereas during active times, their amplitudes are the largest in the sector from dawn and noon (indicated by Figures 2b, 2c, 2h, and 2i).

However, the WNAs of plasmaspheric hiss have little dependence on substorm activity (*AE*) in most regions. The intense substorm activities ($AE \geq 300$ nT) mainly lead to the increase of hiss WNAs in the nightside low *L*-region ($MLT \sim 22:00\text{--}02:00$ and $L \leq 4$ in Figures 2f and 2l). During different substorm intensities, the equatorial hiss WNAs ($|MLAT| \leq 10^\circ$ in Figures 2d–2f) are still less than those at midlatitudes ($|MLAT| > 10^\circ$ in Figures 2j–2l). The remarkable latitudinal variation of hiss WNAs suggests that the hiss waves gradually become oblique when they propagate from the equatorial region to the middle/high latitudes.

Since the statistical samples of the hiss wave amplitudes in each bin satisfy a power law distribution rather than a normal distribution, a small number of outliers can heavily influence the standard

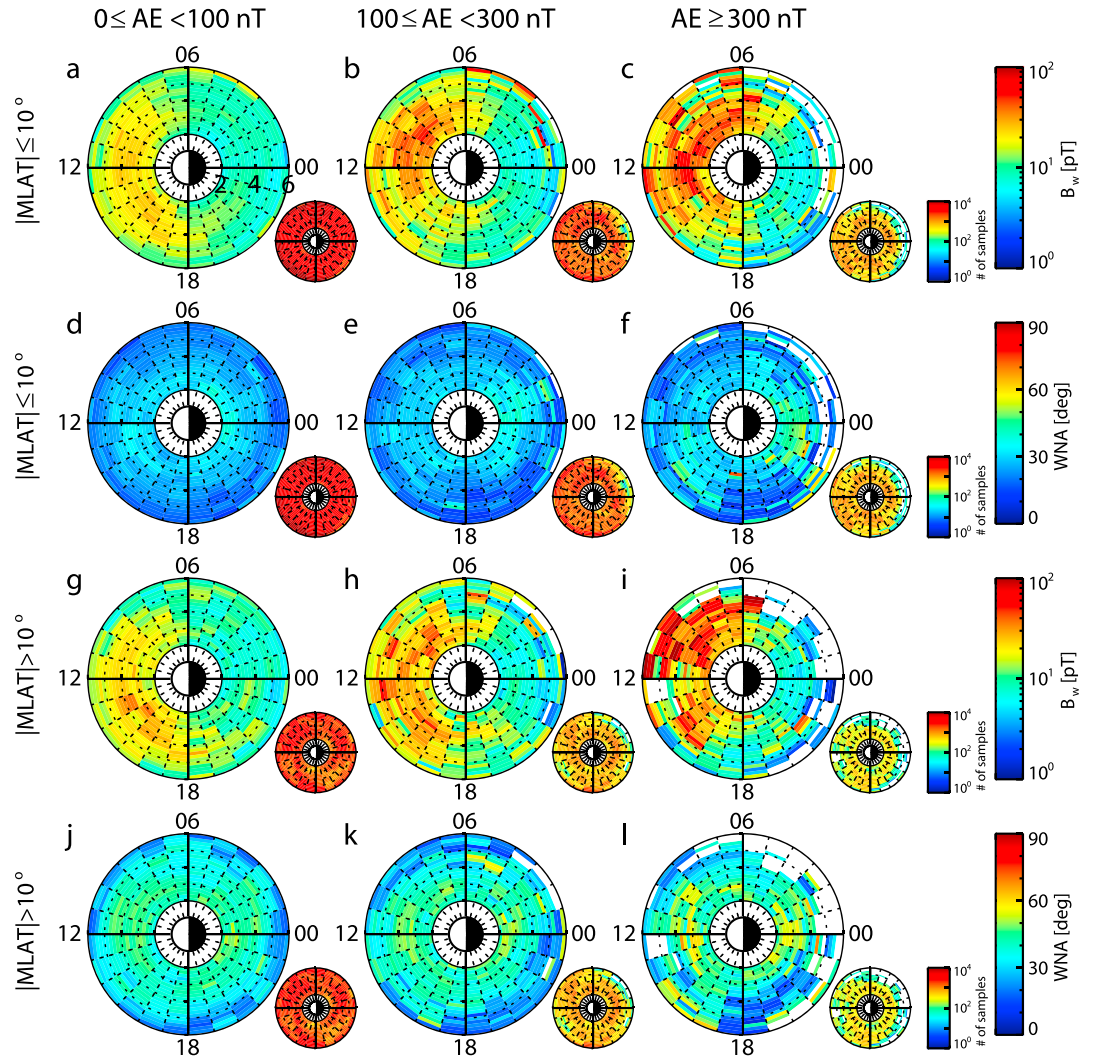


Figure 2. The global (L-MLT) distributions of hiss wave amplitudes (median B_w) and wave normal angles (WNA is the power-weighted average) during different substorm activities (AE).

deviation. However, the deviations of a small number of outliers are irrelevant in the median absolute deviation (MAD), as explanations in the Web (https://en.wikipedia.org/wiki/Median_absolute_deviation). Thus, the MAD is a more robust estimator of the statistical dispersion of the wave amplitude median (B_w) in the non-normal distributed samples. According to the MAD definition [Hampel, 1974], the MAD (ΔB_w) of the hiss wave amplitudes in each bin can be expressed as

$$\Delta B_w = \text{median}(|B_{wi} - \text{median}(B_{wi})|) \quad (4)$$

Unlike the median amplitude of hiss waves, its wave normal angle (WNA) is a power-weighted average (WNA) in each bin. Therefore, the power-weighted standard deviation (ΔWNA) is used to indicate the quality of WNA and

$$\Delta WNA = \left(\frac{\sum_{i=1}^n \int_{f_{\min}}^{f_{\max}} B_{\text{PSD}}(f) df |_i}{\sum_{i=1}^n \int_{f_{\min}}^{f_{\max}} B_{\text{PSD}}(f) df |_i} (WNA_i - WNA)^2 \right)^{\frac{1}{2}} \quad (5)$$

ΔB_w and ΔWNA are displayed in Figure 3. Like the strong substorm dependence of hiss wave amplitudes (B_w), the MAD (ΔB_w) of the hiss wave amplitudes also increases with increasing AE, especially on

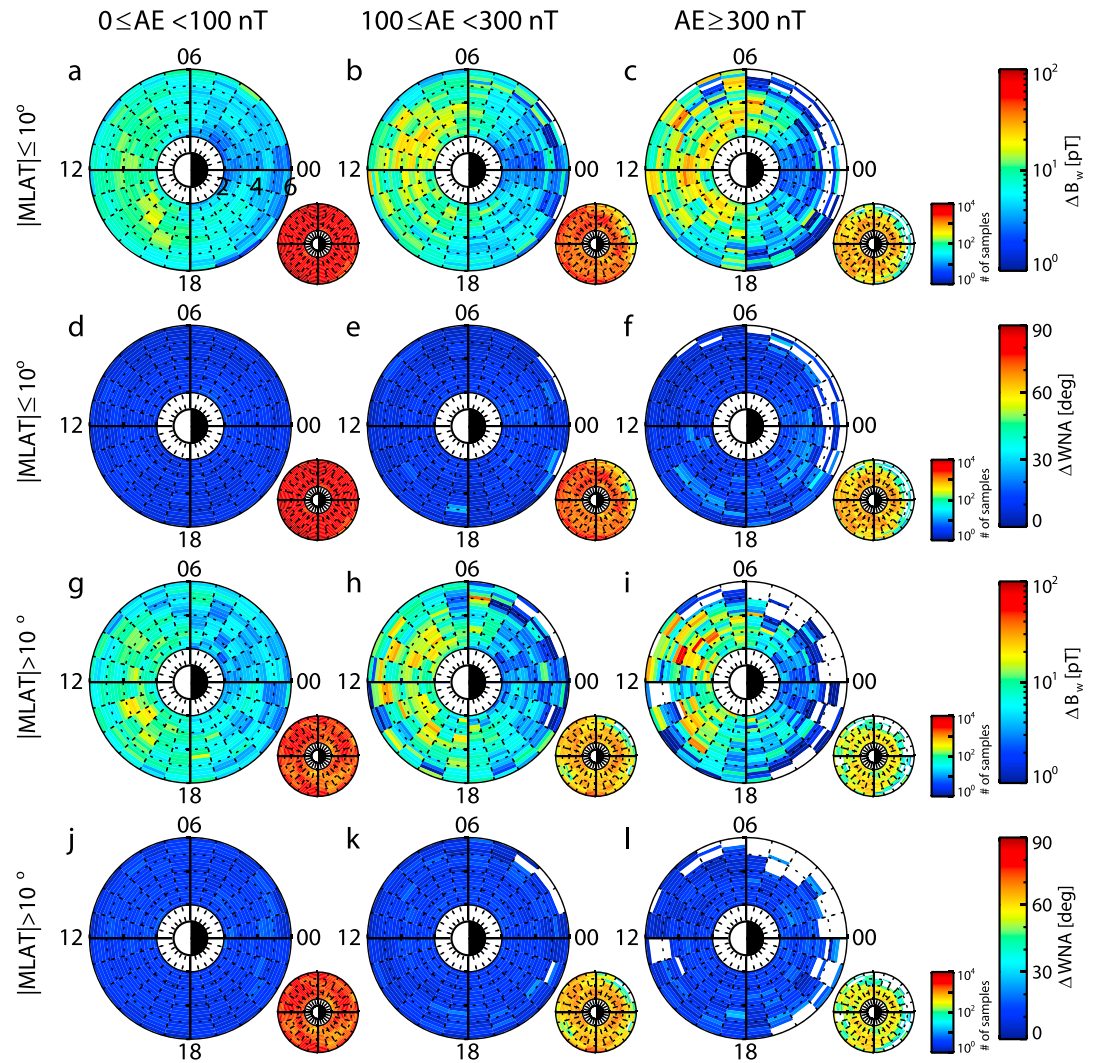


Figure 3. The median absolute deviation (ΔB_w) of hiss wave amplitudes and the standard deviation (ΔWNA) of hiss wave normal angles.

the dayside (indicated by Figures 3a–3c or 3g–3i). However, ΔB_w is smaller than B_w under different AE indices, indicating that the statistical median amplitude (B_w) can well reflect the typical amplitude of hiss waves during different substorm activities. Moreover, the standard deviation (ΔWNA) of global hiss WNAs is also very small under different AE indices. The relatively constant ΔWNA indicate that the spatial distribution of statistical hiss WNAs is reliable, and the substorm influence on hiss WNAs is ignorable in most regions.

In different MLT ranges, the latitudinal distribution of hiss WNAs is also almost independent of substorm activity. Figure 4 shows the latitudinal distribution of hiss WNAs under different AE indices. From the equatorial region ($|MLAT| \leq 10^\circ$) to the midlatitudes ($10^\circ < |MLAT| \leq 20^\circ$), the hiss WNAs increase from 20° to 50° . The latitudinal variation of the observed hiss WNAs can be reproduced through the ray tracing method [Chen et al., 2012]. Figure 5 shows modeled WNA distribution in the prenoon meridional plane with a fixed plasma-pause at $L = 4.5$. Since the plasma densities used in the model cannot completely match with the real plasma environment during the wave observations, there are also small differences between the observed hiss WNAs and the ray-traced results. However, the observed and ray-traced hiss WNAs have similar latitudinal variation tendency, suggesting that the latitudinal variation of the hiss WNAs is probably due to the propagation of waves from the equatorial source region.

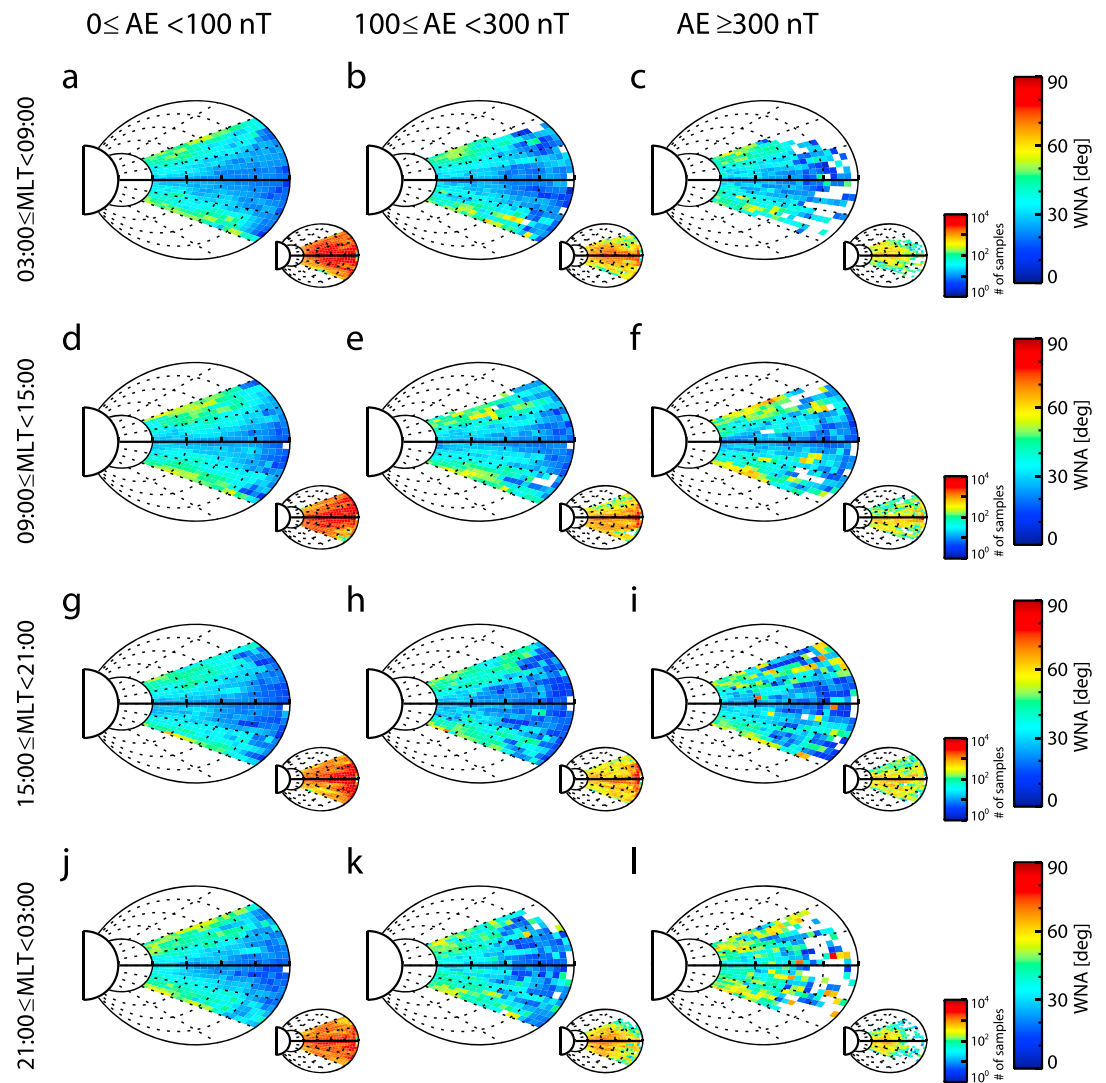


Figure 4. The L-MLAT distribution of hiss wave normal angles (WNAs) during different substorm activities (AE).

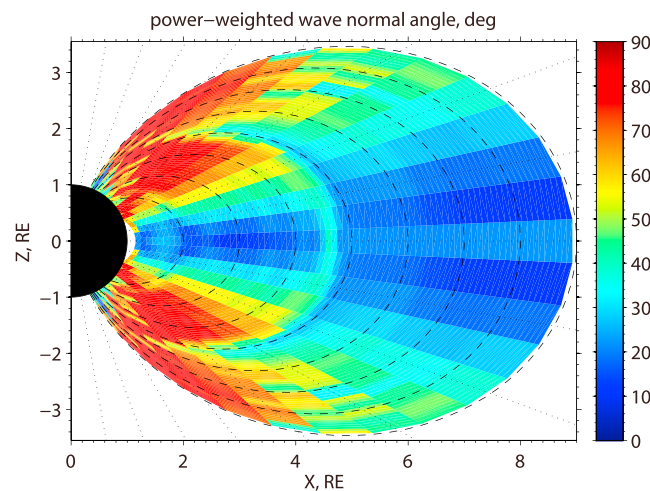


Figure 5. Modeled power-weighted wave normal angles in the meridional plane.

4. Empirical Models

Although the global empirical models of hiss wave amplitudes have been established as a function of Kp index, L, MLT, and MLAT [Spasojevic et al., 2015], the MLAT variation of the wave magnetic field is so small that its latitudinal variation is negligible in the low-latitude range of MLAT < 20°, as indicated by our statistical results (Figure 2). Moreover, the hiss wave amplitudes depend strongly on the intensity of substorm activity (AE or AL) [Li et al., 2015b]. Therefore, we develop a modified empirical model based on the parameters AE, MLT, and L. The hiss wave amplitude ($B_w(AE, L, MLT)$) is expressed as

Table 1. Fitted Coefficients of Global Hiss Wave Amplitudes

a'_0	a'_1	a'_2	
11.7645	0.0221676	-2.33558e-005	
b'_0	b'_1		
0.9804	0.5098		
c'_0	c'_1	c'_2	c'_3
-0.903178	1.43713	-0.323061	0.0219297

$$B_w(AE, L, MLT) = \left(a'_0 + a'_1 AE + a'_2 AE^2 \right) \times \left[b'_0 \sin^2(\alpha/2) + b'_1 \right] \times \left(c'_0 + c'_1 L + c'_2 L^2 + c'_3 L^3 \right) \quad (6)$$

where $\alpha = MLT \times \frac{360}{24} = 15 \times MLT$ and the maximum L-value corresponds to the plasmopause location; other fitting coefficients are shown in Table 1.

Figures 6a–6c show the observed (red circles) and fitted (curve) values of hiss amplitudes as a function of L, MLT, and AE, respectively. The hiss wave amplitudes are the largest in the dayside low L-region ($2 \leq L \leq 4$ and $06:00 \leq MLT \leq 18:00$). This is consistent with the statistical results of Spasojevic et al. [2015]. Furthermore, the global (L-MLT-MLAT) averaged hiss wave amplitude increases with increasing AE.

Besides the wave amplitude influence, the electron pitch angle diffusion coefficient also depends on hiss WNAs during the wave particle resonance [Artemyev et al., 2012; Gao et al., 2015]. Since the small substorm-dependent variation of the hiss WNAs is ignorable in comparison with their large latitudinal variation, the spatial distribution model of global hiss propagation angles (WNAs) can be simplified as a function of spatial location (L, MLT, and MLAT) and

$$\begin{aligned} \tan(WNA(MLAT, MLT, L)) &= (a_0 + a_1 MLAT + a_2 MLAT^2) \times [b_0 \cos(2\alpha) + b_1] \\ &\times (c_0 + c_1 L + c_2 L^2 + c_3 L^3) \end{aligned} \quad (7)$$

where α is the same as that in equation (4) and the maximum L-value also corresponds to the plasmopause location; other fitting coefficients are shown in Table 2.

Figures 6d–6f show the observed (red circles) and fitted (curve) distributions of hiss WNAs as function of L, MLT, and MLAT, respectively. The hiss WNAs decrease with increasing L-value or decreasing MLAT, but their

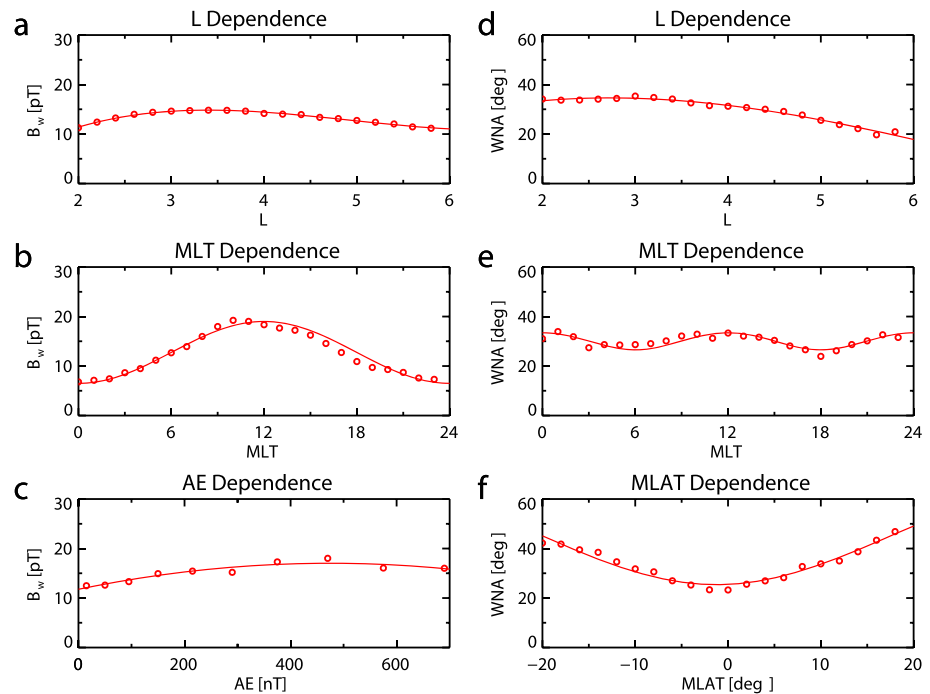


Figure 6. The observed (red circles) and fitted (curve) distributions of hiss amplitudes (B_w) and wave normal angles (WNAs). (a and b) The L and MLT distributions of hiss wave amplitude medians. (c) Hiss wave amplitude medians as a function of AE index. (d–f) The L, MLT, and MLAT distributions of hiss wave normal angles (WNAs).

Table 2. Fitted Coefficients of Global Hiss Wave Normal Angles

a_0	a_1	a_2	
0.4779676	0.0037322	0.0015021	
b_0	b_1		
0.137931	1.00000		
c_0	c_1	c_2	c_3
0.3118320	0.7313696	-0.1760104	0.01016921

observed values in each grid, and their relative errors are less than 20% in most regions. The small relative errors indicate that the fitted equation (7) is reliable. The empirical equation (7) mainly reflects the spatial distribution of global hiss WNAs during relatively weak substorm activity (e.g., $AE < 300$ nT). However, the WNAs of the nightside hiss waves are probably changed during intense substorm activity (e.g., $AE \geq 300$ nT).

5. Discussions

For the first time, we developed a global empirical model (equation (7)) to describe hiss propagation angle variations in the inner magnetosphere ($2 \leq L \leq 6$, $0 \leq \text{MLT} \leq 24$, and $|\text{MLAT}| \leq 20^\circ$). Previous studies just use a Gaussian distribution to fit the wave normal angle range at a fixed spatial location [Glauert and Horne,

MLT variation is very small. The weak MLT variation of the hiss WNAs is also indicated by Figure 7. In Figure 7, the left and middle panels display the observed (WNA_{stat}) and fitted (WNA_{fit}) hiss WNA distributions in the L-MLAT space and the right panels show their relative errors ($(WNA_{stat} - WNA_{fit}) / WNA_{stat} \times 100\%$). The fitted hiss WNAs (WNA_{fit}) can well reproduce the averages (WNA_{stat}) of the

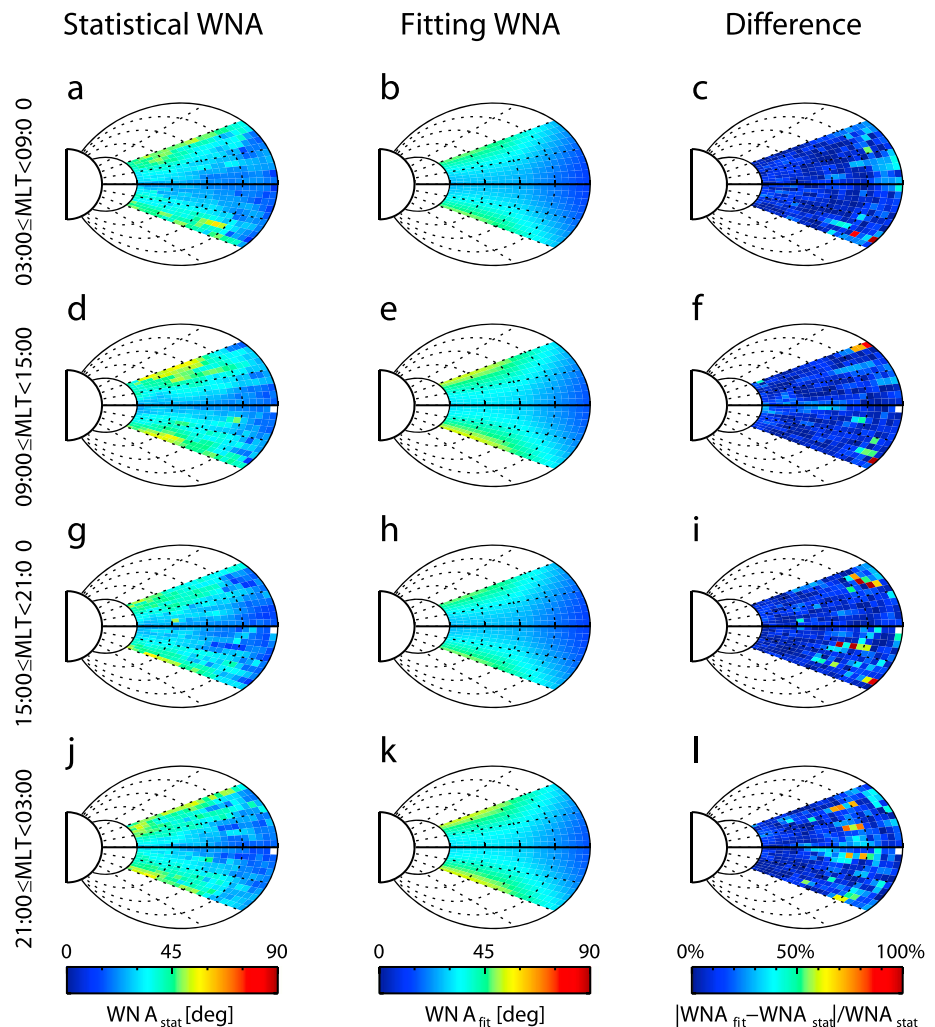


Figure 7. The power-weighted averages (WNA_{stat}) of the satellite observed hiss wave normal angles in each L-MLAT grid, the fitted WNAs (WNA_{fit}), and their relative errors ($(WNA_{stat} - WNA_{fit}) / WNA_{stat} \times 100\%$).

2005]. However, the Gaussian distribution cannot reflect the spatial variation of hiss propagation angles (WNA). Our statistical results indicate that the hiss waves have different peak angles ($X_m = \tan(\text{WNA})$, where $\text{WNA} \sim 10^\circ\text{--}60^\circ$ in Figure 2) at different locations, but their standard deviations are relatively invariant ($X_w = \tan(\Delta\text{WNA})$, where $\Delta\text{WNA} \leq 30^\circ$ in Figure 3). These results are useful to determine different Gaussian distributions at different spatial locations.

Van Allen Probe A observations (Figure 2) indicate that plasmaspheric hiss can exist in a wide L-range ($L \sim 2\text{--}6$) on the dayside during different-intensity substorm activities, but the hiss waves are lacking in the nightside high L-region ($L > 5$) during intense substorm activity ($AE \geq 300$ nT). These results are similar to the statistical results of *Li et al.* [2015b]. Previous observations and simulations indicate that the dayside plasmasphere/plume (i.e., the hiss emission region) can exist at high L-shells (e.g., $L \sim 6$) under different geomagnetic conditions [*Jordanova et al.*, 2007]. Since the irregular structure (plume) of the dayside plasmasphere can appear at high L-shells at different MLTs during active times, the statistical averaged L-value range of the dayside hiss emission region has no evident substorm (AE) dependence. However, the enhanced geomagnetic activities can cause the earthward movement of the nightside plasmopause ($L_{pp} \sim 4\text{--}5$ during the shrinkage of plasmasphere) [*Jordanova et al.*, 2007]. Thus, there is no hiss wave in the nightside high L-region ($L > 5$) outside the plasmopause during intense substorm activity ($AE \geq 300$ nT). Interestingly, the enhanced substorm activity causes the hiss WNA enlargement in the nightside low L-region ($2 \leq L \leq 4$ and $21:00 \leq \text{MLT} \leq 03:00$), suggesting that the hiss waves in the nightside low L-region probably originate from the penetration of chorus waves from the high L-region. This is consistent with the observation result of *Li et al.* [2015a].

However, the enhanced substorm activity (the increasing AE) does not effectively change the hiss WNAs on the dayside (MLT $\sim 06:00\text{--}18:00$); it mainly leads to the amplification of the dayside hiss amplitudes. The relatively stable hiss WNAs on the dayside suggest that the dayside hiss waves probably originate from multiple sources, such as the combined hiss amplifications through the cyclotron resonance with anisotropic suprathermal electrons and the penetration of chorus waves [*Chen et al.*, 2012].

6. Summary and Conclusions

By processing the wave data measured by the EMFISIS instrument on board Van Allen Probe A, we obtain the spatial distributions of hiss wave amplitudes and wave normal angles (WNAs) during different-intensity substorm activities. The hiss wave amplitudes have a day-night asymmetry and a strong dependence on substorm activity. The amplitudes of the dayside hiss waves increase when substorm activity is enhanced (AE increases), and the dayside hiss amplitudes are greater than the nightside. However, the propagation angles (WNAs) of hiss waves in most regions have no strong dependence on substorm activity. The intense substorm activity ($AE \geq 300$ nT) merely causes the hiss WNA enlargement in the nightside low L-region (MLT $\sim 22:00\text{--}02:00$ and $L \leq 4$).

During different-intensity substorm activities, the propagation angles of hiss waves display significantly latitudinal and radial variations. The equatorial hiss WNAs ($|\text{MLAT}| \leq 10^\circ$) are generally less than or equal to 30° , whereas the midlatitude hiss WNAs ($|\text{MLAT}| > 10^\circ$) are mostly greater than 30° in the plasmaspheric region of $L \leq 5$. At different MLTs, the hiss WNAs tend to increase with decreasing radial distance (i.e., the decreasing L-value). The spatial distribution of hiss WNAs is consistent with the ray tracing result of hiss propagation process. The spatial variation of hiss WNAs is probably due to the wave propagation or different sources.

Based on the Van Allen Probe observations, we develop the first empirical model to describe the hiss propagation angle variations inside the plasmasphere ($2 \leq L \leq 6$, $0 \leq \text{MLT} \leq 24$, and $|\text{MLAT}| \leq 20^\circ$). The fitted hiss WNAs can well reproduce the averages of the observed values in each grid, and their relative errors are less than 20% in most regions. Meanwhile, we also develop another empirical model to describe the global hiss wave amplitude variations during different-intensity substorm activities.

References

- Agapitov, O., A. Artemyev, V. Krasnoselskikh, Y. V. Khotyaintsev, D. Mourenas, H. Breuillard, M. Balikhin, and G. Rolland (2013), Statistics of whistler-mode waves in the outer radiation belt: Cluster STAFF-SA measurements, *J. Geophys. Res. Space Physics*, 118, 3407–3420, doi:10.1002/jgra.50312.

Acknowledgments

This work is supported by the NSFC (41374165, 41431071, and 41074119). LC acknowledge the NSF grant 1405041 through the Geospace Environment Modeling program, and the AFOSR grant of FA9550-16-1-0344. Van Allen Probe data are available at the Web <https://emfisis.physics.uiowa.edu/>. Geomagnetic indices (AE) are available at the Web http://cdaweb.gsfc.nasa.gov/sp_phys. The authors thank EMFISIS group and other staff working for these data.

- Artemyev, A., O. Agapitov, H. Breuillard, V. Krasnoselskikh, and G. Rolland (2012), Electron pitch-angle diffusion in radiation belts: The effects of whistler wave oblique propagation, *Geophys. Res. Lett.*, *39*, L08105, doi:10.1029/2012GL051393.
- Bortnik, J., R. M. Thorne, and N. P. Meredith (2008), The unexpected origin of plasmaspheric hiss from discrete chorus emissions, *Nature*, *452*, 62, doi:10.1038/nature06741.
- Cao, J. B., et al (2005), First results of Low Frequency Electromagnetic Wave Detector (LFEW) of TC-2/Double Star program, *Ann. Geophys.*, *23*(8), 2803–2811, doi:10.5194/angeo-23-2803-2005.
- Cao, J. B., J. Y. Yang, C. X. Yan, and L. Y. Li (2007), The observations of high energy electrons and associated waves by DSP satellites during substorm, *Nuclear Physics B Suppl.*, *166*, 56–61, doi:10.1016/j.nuclphysbps.2006.12.066.
- Chan, K.-W., and R. E. Holzer (1976), ELF hiss associated with plasma density enhancements in the outer magnetosphere, *J. Geophys. Res.*, *81*, 2267–2274, doi:10.1029/JA081i013p02267.
- Chen, L., W. Li, J. Bortnik, and R. M. Thorne (2012), Amplification of whistler-mode hiss inside the plasmasphere, *Geophys. Res. Lett.*, *39*, L08111, doi:10.1029/2012GL051488.
- Gao, Y., F. Xiao, Q. Yan, C. Yang, S. Liu, Y. He, and Q. Zhou (2015), Influence of wave normal angles on hiss-electron interaction in Earth's slot region, *J. Geophys. Res. Space Physics*, *120*, 9385–9400, doi:10.1002/2015JA021786.
- Glauert, S. A., and R. B. Horne (2005), Calculation of pitch angle and energy diffusion coefficients with the PADIE code, *J. Geophys. Res.*, *110*, A04206, doi:10.1029/2004JA010851.
- Hampel, F. R. (1974), The influence curve and its role in robust estimation, *J. Am. Stat. Assoc.*, *69*(346), 383–393, doi:10.1080/01621459.1974.10482962.
- Jordanova, V. K., M. Spasojevic, and M. F. Thomsen (2007), Modeling the electromagnetic ion cyclotron wave-induced formation of detached subauroral proton arcs, *J. Geophys. Res.*, *112*, A08209, doi:10.1029/2006JA012215.
- Kim, K.-C., D.-Y. Lee, and Y. Shprits (2015), Dependence of plasmaspheric hiss on solar wind parameters and geomagnetic activity and modeling of its global distribution, *J. Geophys. Res. Space Physics*, *120*, 1153–1167, doi:10.1002/2014JA020687.
- Kletzing, C. A., et al. (2013), The Electric and Magnetic Field Instrument Suite and Integrated Science (EMFISIS) on RBSP, *Space Sci. Rev.*, *179*, 127–181, doi:10.1007/s11214-013-9993-6.
- Kurth, W. S., S. De Pascuale, J. B. Faden, C. A. Kletzing, G. B. Hospodarsky, S. Thaller, and J. R. Wygant (2015), Electron densities inferred from plasma wave spectra obtained by the waves instrument on Van Allen Probes, *J. Geophys. Res. Space Physics*, *120*, 904–914, doi:10.1002/2014JA020857.
- Li, L. Y., J. B. Cao, and G. C. Zhou (2008), Whistler-mode waves modify the high-energy electron slot region and the outer radiation belt [in Chinese], *Chin. J. Geophys.*, *51*(2), 316–324.
- Li, L. Y., J. B. Cao, G. C. Zhou, and X. Li (2009), Statistical roles of storms and substorms in changing the entire outer zone relativistic electron population, *J. Geophys. Res.*, *114*, A12214, doi:10.1029/2009JA014333.
- Li, L. Y., J. Yu, J. B. Cao, D. Zhang, X. H. Wei, Z. J. Rong, J. Y. Yang, and H. S. Fu (2013), Rapid loss of the plasma sheet energetic electrons associated with the growth of whistler mode waves inside the bursty bulk flows, *J. Geophys. Res. Space Physics*, *118*, 7200–7210, doi:10.1002/2013JA019109.
- Li, W., R. M. Thorne, N. P. Meredith, R. B. Horne, J. Bortnik, Y. Y. Shprits, and B. Ni (2008), Evaluation of whistler mode chorus amplification during an injection event observed on CRRES, *J. Geophys. Res.*, *113*, A09210, doi:10.1029/2008JA013129.
- Li, W., et al. (2014), Evidence of stronger pitch angle scattering loss caused by oblique whistler-mode waves as compared with quasi-parallel waves, *Geophys. Res. Lett.*, *41*, 6063–6070, doi:10.1002/2014GL061260.
- Li, W., L. Chen, J. Bortnik, R. M. Thorne, V. Angelopoulos, C. A. Kletzing, W. S. Kurth, and G. B. Hospodarsky (2015a), First evidence for chorus at a large geocentric distance as a source of plasmaspheric hiss: Coordinated THEMIS and Van Allen Probes observation, *Geophys. Res. Lett.*, *42*, 241–248, doi:10.1002/2014GL062832.
- Li, W., Q. Ma, R. M. Thorne, J. Bortnik, C. A. Kletzing, W. S. Kurth, G. B. Hospodarsky, and Y. Nishimura (2015b), Statistical properties of plasmaspheric hiss derived from Van Allen Probes data and their effects on radiation belt electron dynamics, *J. Geophys. Res. Space Physics*, *120*, 3393–3405, doi:10.1002/2015JA021048.
- Li, L. Y., J. Yu, J. B. Cao, and Z. G. Yuan (2016), Compression-amplified EMIC waves and their effects on relativistic electrons, *Phys. Plasmas*, *23*, 062116, doi:10.1063/1.4953899.
- Lyons, L. R., R. M. Thorne, and C. F. Kennel (1972), Pitch angle diffusion of radiation belt electrons within the plasmasphere, *J. Geophys. Res.*, *77*, 3455–3474, doi:10.1029/JA077i019p03455.
- Ma, Q., W. Li, R. M. Thorne, J. Bortnik, C. A. Kletzing, W. S. Kurth, and G. B. Hospodarsky (2016), Electron scattering by magnetosonic waves in the inner magnetosphere, *J. Geophys. Res. Space Physics*, *121*, 274–285, doi:10.1002/2015JA021992.
- Meredith, N. P., R. B. Horne, R. M. Thorne, D. Summers, and R. R. Anderson (2004), Substorm dependence of plasmaspheric hiss, *J. Geophys. Res.*, *109*, A06209, doi:10.1029/2004JA010387.
- Meredith, N. P., R. B. Horne, S. A. Glauert, and R. R. Anderson (2007), Slot region electron loss timescales due to plasmaspheric hiss and lightning-generated whistlers, *J. Geophys. Res.*, *112*, A08214, doi:10.1029/2007JA012413.
- Meredith, N. P., R. B. Horne, A. Sicard-Piet, D. Boscher, K. H. Yearby, W. Li, and R. M. Thorne (2012), Global model of lower band and upper band chorus from multiple satellite observations, *J. Geophys. Res.*, *117*, A10225, doi:10.1029/2012JA017978.
- Ni, B., et al. (2014), Resonant scattering of energetic electrons by unusual low frequency hiss, *Geophys. Res. Lett.*, *41*, 1854–1861, doi:10.1002/2014GL059389.
- Santolik, O., M. Parrot, and F. Lefeuvre (2003), Singular value decomposition methods for wave propagation analysis, *Radio Sci.*, *38*(1), 1010, doi:10.1029/2000RS002523.
- Spasojevic, M., Y. Y. Shprits, and K. Orlova (2015), Global empirical models of plasmaspheric hiss using Van Allen Probes, *J. Geophys. Res. Space Physics*, *120*, 10,370–10,383, doi:10.1002/2015JA021803.
- Summers, D., B. Ni, and N. P. Meredith (2007a), Timescales for radiation belt electron acceleration and loss due to resonant wave-particle interactions: 1. Theory, *J. Geophys. Res.*, *112*, A04206, doi:10.1029/2006JA011801.
- Summers, D., B. Ni, and N. P. Meredith (2007b), Timescales for radiation belt electron acceleration and loss due to resonant wave-particle interactions: 2. Evaluation for VLF chorus, ELF hiss, and electromagnetic ion cyclotron waves, *J. Geophys. Res.*, *112*, A04207, doi:10.1029/2006JA011993.
- Thorne, R. M., et al. (2013), Evolution and slow decay of an unusual narrow ring of relativistic electrons near $L \sim 3.2$ following the September 2012 magnetic storm, *Geophys. Res. Lett.*, *40*, 3507–3511, doi:10.1002/grl.50627.
- Tu, W., G. S. Cunningham, Y. Chen, M. G. Henderson, E. Camporeale, and G. D. Reeves (2013), Modeling radiation belt electron dynamics during GEM challenge intervals with the DREAM3D diffusion model, *J. Geophys. Res. Space Physics*, *118*, 6197–6211, doi:10.1002/jgra.50560.

- Xiao, F., Z. Su, H. Zheng, and S. Wang (2010), Three-dimensional simulations of outer radiation belt electron dynamics including cross diffusion terms, *J. Geophys. Res.*, *115*, A05216, doi:10.1029/2009JA014541.
- Yu, J., L. Y. Li, J. B. Cao, Z. G. Yuan, G. D. Reeves, D. N. Baker, J. B. Blake, and H. Spence (2015), Multiple loss processes of relativistic electrons outside the heart of outer radiation belt during a storm sudden commencement, *J. Geophys. Res. Space Physics*, *120*, 10,275–10,288, doi:10.1002/2015JA021460.
- Zhima, Z., J. Cao, W. Liu, F. Huishan, J. Yang, X. Zhang, and X. Shen (2013), DEMETER observations of high latitude chorus waves penetrating the plasmasphere during a geomagnetic storm, *Geophys. Res. Lett.*, *40*, 5827–5832, doi:10.1002/2013GL058089.